Anisotropy in the Turbulent Flow through Random and Emergent Rigid Vegetation on Rough Beds

N. Penna & F. Coscarella
Dipartimento di Ingegneria Civile, Università della Calabria, Rende (CS), Italy

P. Gualtieri
Dipartimento di Ingegneria Civile, Edile e Ambientale, Università degli Studi di Napoli "Federico II", Naples (NA), Italy

R. Gaudio
Dipartimento di Ingegneria Civile, Università della Calabria, Rende (CS), Italy

ABSTRACT: In this study, we explore for the first time the turbulence anisotropy of flows through random and emergent rigid vegetation on rough beds, using the anisotropy invariant maps (AIMs). We present the results of an experimental campaign, based on Acoustic Doppler Velocimeter (ADV) measures, varying the bed sediment size (coarse sand, fine gravel, and coarse gravel), under the same hydraulic conditions. The evolution of the stress ellipsoid formed by the Reynolds stresses is discussed, together with the analysis of the anisotropic invariant function. We demonstrate that vegetation distribution is of paramount importance in the turbulence anisotropy evolution along the water depth. While in the case of a regular pattern the bed roughness is the key parameter in determining the shape of the stress ellipsoid in the near-bed region, in a random vegetation distribution this assumption is no longer valid. However, by increasing the bed roughness in such kind of arrangement, its effect on the turbulence anisotropy are visible in specific areas around the vegetation stem. This is confirmed by the analysis of the anisotropic invariant function calculated for different sections close to the stem itself.

1 INTRODUCTION

One of the most frequently analyzed quantities in hydrodynamic studies is the anisotropic behavior of turbulence, in terms of the degree of departure from the isotropic turbulence. Specifically, turbulence is isotropic when the velocity fluctuations are the same regardless of the rotation of axes (Sarkar et al. 2019). Hence, the Reynolds normal stresses (σ_{uu}, σ_{vv}, and σ_{ww}, in the streamwise, spanwise, and vertical directions, respectively) can be considered invariant. On the contrary, turbulence is anisotropic when the Reynolds normal stresses vary with the directions, i.e. the temporal velocity fluctuations have a preferential direction with respect to the others.

The Reynolds stress anisotropy tensor is the most convenient tool to characterize anisotropy in turbulent flows, by using the anisotropic invariant map (AIM), also called the Lumley triangle. It was originally introduced by Lumley & Newman (1977) and it is the representation of a two-dimensional domain based on the invariant properties of the Reynolds stress anisotropy tensor b_{ij}:

$$b_{ij} = \frac{\overline{u'_i u'_j}}{\overline{u'_i u'_i}} - \frac{1}{3}\delta_{ij} \tag{1}$$

where the apex indicates the velocity fluctuation, $\overline{u'_i u'_i}$ is twice the turbulent kinetic energy (TKE), adopting the Einstein notation, and δ_{ij} is the Kronecker delta function (if $i = j$, $\delta_{ij} = 1$, otherwise $\delta_{ij} = 0$). Thus, the AIM appears like a triangle (Fig. 1) on a (*III*, -*II*) plane, where *II* indicates the anisotropy degree and *III* the nature of anisotropy, whose boundaries are characteristic of the turbulent state (1D, 2D, or 3D turbulence) and processes (axisymmetric expansion, axisymmetric contraction, and two component turbulence) (Dey et al. 2020). Specifically, *II* and

III are the second and third invariants of the Reynolds stress anisotropy tensor, respectively, which are expressed as follows:

$$II = -\frac{b_{ij}b_{ij}}{2} = -\left(\lambda_1^2 + \lambda_1\lambda_2 + \lambda_2^2\right) \tag{2}$$

$$III = \frac{b_{ij}b_{jk}b_{ki}}{3} = -\lambda_1\lambda_2(\lambda_1 + \lambda_2) \tag{3}$$

where λ_1 and λ_2 are the anisotropy eigenvalues.

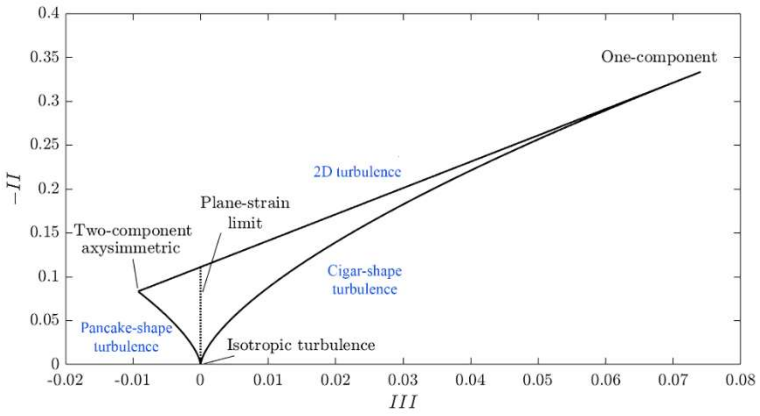

Figure 1. Conceptual diagram of the anisotropy invariant map.

The left curve of the AIM is described by the function $III = -2(-II/3)^{3/2}$. In this case, two diagonal components of the Reynolds stress tensor are greater than the other one and turbulence is defined as pancake-shaped. The resulting stress ellipsoid is, therefore, an oblate spheroid, in which $\sigma_{uu} = \sigma_{vv} > \sigma_{ww}$. The left vertex of the curve determines the two-component axisymmetric limit and the stress ellipsoid is a circular disk ($\sigma_{uu} = \sigma_{vv}$, and $\sigma_{ww} = 0$). Instead, the right curve indicates the case in which only one component of the Reynolds stress tensor is greater than the other two, thus turbulence is cigar-shaped and the stress ellipsoid is a prolate spheroid ($\sigma_{uu} = \sigma_{vv} < \sigma_{ww}$). The right vertex of the curve represents the one component limit and the stress ellipsoid is a straight line ($\sigma_{uu} > 0$ and $\sigma_{vv} = \sigma_{ww} = 0$, or $\sigma_{ww} > 0$ and $\sigma_{uu} = \sigma_{vv} = 0$). The right curve of the AIM is defined by the following relationship: $III = 2(-II/3)^{3/2}$. The upper line of the AIM corresponds to the 2D turbulence, in which the stress ellipsoid shape is like that of an elliptical disk ($\sigma_{uu} > \sigma_{vv}$, and $\sigma_{ww} = 0$), and it is expressed as follows: $III = -(9II+1)/27$. Finally, the bottom cusp of the AIM is related to the 3D isotropic turbulence. In this case the stress ellipsoid is a sphere ($\sigma_{uu} = \sigma_{vv} = \sigma_{ww}$).

Turbulence anisotropy is a common feature of complex fluid flows, such as those characterizing vegetated channels (Emory & Iaccarino 2014). Using the AIMs, Caroppi et al. (2018) analyzed the effects of submerged vegetation (made of rigid cylinders) on the flow turbulent structures on a smooth bed. They showed that a two-component isotropic turbulence was present in the viscous sublayer (directly above the flume bed). However, moving upwards, at the top of the canopy, the turbulence reached a quasi-1D state. Above the canopy, turbulence moved through the axisymmetric expansion, tending to a 2D isotropic state. More recently, Penna et al. (2020) investigated the anisotropy of turbulent flows through an array of cylinders with an aligned pattern simulating rigid vegetation on rough beds. They observed that, in the presence of such an arrangement, the effect of both vegetation and bed roughness causes the evolution of the turbulence from the axisymmetric anisotropy to the quasi-3D isotropy approaching the water surface. This behavior was particularly evident for the finest bed sediment diameter used in their experiments. Finally, Barman & Kumar (2022) studied the turbulence anisotropy in a compound channel with the combination of submerged and emergent vegetation. They observed that the main channel section of 67% emergent vegetation case had a greater tendency to approach 2D turbulence than other non-uniform vegetation setups.

Since the Reynolds stress anisotropy reflects, to a large extent, the presence of organized motions, being the only part of the total stress responsible for the momentum transport (Pope 2000), its study is crucial for the understanding and modeling of turbulence (Caroppi et al. 2018), as well as of sediment transport processes (Penna et al. 2022), in vegetated flows.

Hence, the driving idea of the present study is the description of the turbulence anisotropy, through the AIMs, of turbulent flow through random and emergent rigid vegetation on rough beds, highlighting the effect of both roughness and vegetation distribution.

2 EXPERIMENTS AND METHODOLOGY

2.1 *Laboratory flume, vegetation and bed sediments*

The experimental campaign was carried out in the *Laboratorio* "*Grandi Modelli Idraulici*" (GMI) of the *Università della Calabria* (Italy), in a recirculating rectangular 9.66 m-long, 48.5 cm-wide tilting flume, randomly and densely vegetated.

A submerged pump supplied the flow discharge Q equal to 19.73 l /s. At the inlet of the channel, in order to reduce the influence of the pump on the turbulence characteristics of the flow, honeycombs of 10 mm in diameter were installed. Instead, the flow discharge was measured at the flume outlet using a V-notch weir mounted in a downstream tank. The water depth h within the flume was regulated using a tailgate and measured with a point gauge (equipped with a decimal Vernier) 50 cm upstream of the vegetation array. This latter was placed 6.04 m downstream of the flume inlet. The experiments were performed with h = 0.12 m, resulting in an approaching cross-section average flow velocity equal to $U = Q/(Bh)$ = 0.34 m/s, B being the flume width. The longitudinal flume slope was fixed using a hydraulic jack at 0.15%.

The rigid vegetation was simulated with 68 vertical, wooden and circular cylinders, having height and diameter of 0.40 m and 0.02 m, respectively. Therefore, the experimental tests were performed with emergent vegetation. The cylinders, randomly arranged, were fixed to a 1.96 m-long, 0.485 m-wide and 0.015 m-thick Plexiglas panel and, hence, to the flume bottom. The frontal area per vegetation volume and the solid volume fraction occupied by the cylinders were equal to $a = nd$ = 1.4 m^{-1} and $\varphi = \pi ad/4$ = 0.02, respectively, where n is the number of cylinders per bed area (=71 m^{-2}) and d is the cylinder diameter. Thus, according to Nepf (2012), the vegetation can be considered as dense.

The flume bed was, successively, covered with a layer of uniform very coarse sand (d_{50} = 1.53 mm, where d_{50} is the sediment median diameter), fine gravel (d_{50} = 6.49 mm), and coarse gravel (d_{50} = 17.98 mm), to perform Runs 1, 2, and 3, respectively. Specifically, sediments within the flume were screeded to guarantee the same slope of the bed as that of the flume bottom.

2.2 *Experimental procedure*

Table 1 shows a summary of the experimental settings adopted in each run. Note that all the experiments were performed under the same hydraulic conditions, varying only the bed sediments (i.e. the bed roughness), to highlight their effects, combined with those related to the cylinders, on the turbulence anisotropy. Along with the d_{50}, the other listed variables in Table 1 are the following: the shear velocity, u_*; the water temperature, T; the water kinematic viscosity, ν, which depends on T (Julien 2010); the flow Froude number, $Fr = U/(gh)^{0.5}$, where g is the gravity acceleration; the flow Reynolds number, $Re = Uh/\nu$; the shear Reynolds number, $Re_* = u_*\varepsilon/\nu$, where ε is the Nikuradse equivalent sand roughness, equal to $2d_{50}$; the Reynolds number of the cylinders, $Re_d = Ud/\nu$. As regards the shear velocity, it was calculated by linearly extending the distribution of the turbulent shear stress down to the crest level, measured 50 cm upstream of the vegetation array, namely in undisturbed flow conditions. Hence, $u_* = (-\overline{u'w'})^{0.5}$, where u' and w' are the temporal velocity fluctuations in the streamwise and vertical directions, respectively, whereas the overbar indicates the time average.

An Acoustic Doppler Velocimeter (ADV) profiler with a four-beam down-looking probe (Nortek Vectrino) was used to capture the instantaneous velocity components (streamwise u, spanwise v, and vertical w). The measurements were performed within the study area shown in Figure 2, along three different longitudinal sections, distant 1 cm each other, at the following streamwise distances: x/L_s = 0, 0.17, 0.33, 0.67, 0.83, and 1.00, where x is the streamwise ab-

scissa and L_s is the length of the study area, equal to 12 cm. Note that the longitudinal section (Section 3 in Fig. 2) corresponds to the flume centerline. Here, only two points were measured, owing to the physical impediment related to the ADV in the vicinity of the vegetation stem. Also, two cross-sections 5 cm upstream and downstream of the vegetation stem, respectively, were investigated, considering the following spanwise distances: y/B_s = 0, 0.17, 0.25, 0.33, 0.50, 0.67, 0.75, 0.83, and 1.00, where y is the spanwise coordinate (from the left to the right flume sidewall) and B_s is the width of the study area, equal to 12 cm. Hence, for all the runs, a total number of 26 velocity profiles was captured. The vertical spatial resolution was 3 mm for $z \leq 15$ mm and 5 mm for $z > 15$ mm, where z is the vertical coordinate starting from the maximum crest level in the study area. Since the ADV beams converge at 5 cm below the probe, it was not possible to measure the flow velocity within the flow zone 5 cm below the water surface.

Table 1. Summary of the experimental conditions.

Run	d_{50} (mm)	u_* (m/s)	T (°C)	ν (m^2/s)	Fr (-)	Re (-)	Re_* (-)	Re_d (-)
1	1.53	0.021	16.67	1.09×10^{-6}	0.31	37,431	59	6239
2	6.49	0.022	18.06	1.05×10^{-6}	0.31	38,857	272	6192
3	17.98	0.028	18.70	1.03×10^{-6}	0.31	39,612	978	6602

The instrument sampling frequency was 100 Hz, and the duration of a single sampling was 300 s, for a total number of 30,000 samples, which is adequate to determine accurate turbulence statistics (e.g. Dey & Das 2012, Strom & Papanicolau 2007). The ADV raw data were prefiltered, discarding the values with correlation (COR) lower than 70% and a signal-to-noise ratio (SNR) lower than 15 dB. Subsequently, before processing the ADV data for the analysis, spikes were detected by applying the phase-space thresholding method (Goring & Nikora 2002) and replaced by a third-order polynomial through 12 points on both sides of the spikes.

Further details on the experimental procedure were recently reported by Coscarella et al. (2021).

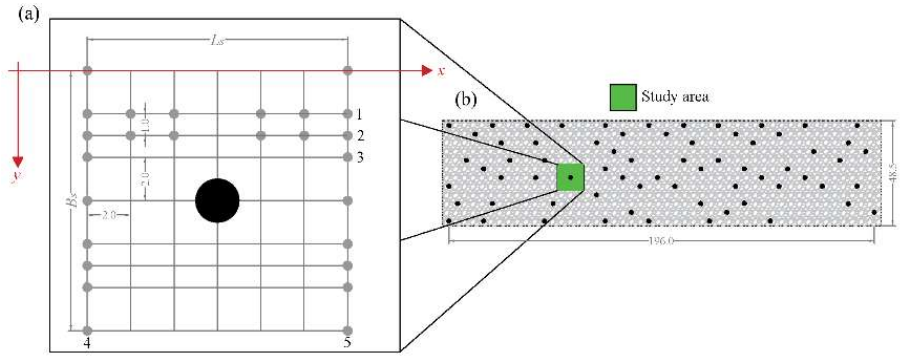

Figure 2. Plan view of the cylinder array within the flume and measurement points within the study area (dimensions are in cm).

3 RESULTS AND DISCUSSION

3.1 *Anisotropy invariant maps*

Figure 3 shows the AIMs and data plots of $-II$ and III for Run 1 at Section 3. Similarly, the AIMs of Sections 4 and 5 of Run 1 are depicted in Figures 4 and 5, respectively. Each subplot indicates the evolution of the turbulence anisotropy along the dimensionless vertical distance $\hat{z} = z/h$.

Looking at Figure 3a, upstream and on the left side of the cylinder, moving from the crest level upwards, the data starting from the plane-strain limit (the dotted line in the figure) shows a feeble tendency toward the left curve of the AIM and, therefore, to the pancake-shaped turbulence. As the vertical distance increases, in the region less affected by the roughness, turbulence

tends to the 3D isotropy, with $\sigma_{uu} = \sigma_{vv} = \sigma_{ww}$, through an axisymmetric contraction. A slightly different behavior can be seen in Figure 3b, that is downstream of and at the left side of the cylinder: data moves from the plane-strain limit directly toward the cusp. Considering that Figure 3 refers to the flume centerline, we can postulate that the vegetation arrangement controls the evolution of the turbulence anisotropy also near the bed, where the effect of bed roughness should be predominant. In fact, in the same hydraulic, vegetation density, and roughness conditions, with an aligned and regular pattern of vegetation, Penna et al. (2020) obtained a different result: in the near-bed region, the stress ellipsoid was a prolate spheroid, and thus turbulence was cigar-shaped.

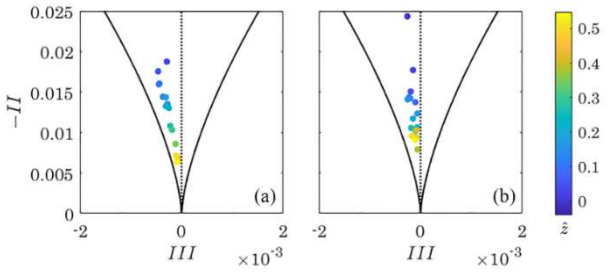

Figure 3. AIMs of Run 1 at Section 3 ($y/B_s = 0.33$): (a) $x/L_s = 0$, and (b) 1.00.

Figures 4 and 5, instead, show that the upstream and downstream of the vegetation stem turbulence behaves in an opposite way. Specifically, at $x/L_s = 0$ and $y/B_s = 0$ (Fig. 4a), it is clear that turbulence is always pancake-shaped, regardless of the vertical distance from the bed. At the same time, at $x/L_s = 1$ and $y/B_s = 0$ (Fig. 5a), turbulence is initially cigar-shaped, and, as one moves toward the free surface, it tends to reach the 3D isotropy through an axisymmetric expansion. Immediately upstream of the cylinder ($x/L_s = 0$, $y/B_s = 0.5$), Figure 4b shows a similar trend: a weak cigar-shaped turbulence near the bed, that tends to the 3D isotropy as z increases. However, at $x/L_s = 1$ and $y/B_s = 0.5$ (Fig. 5b), the stress ellipsoid is basically an oblate spheroid at each elevation from the bed. Finally, at $x/L_s = 0$ and $y/B_s = 1$ (Fig. 4c), moving from the crest level upwards, the data starts from the plane-strain limit and, then, shows a feeble tendency toward the right curve of the AIM and, successively, to the 3D isotropy. Instead, at $x/L_s = 1$ and $y/B_s = 1$ (Fig. 5c), data moves from the plane-strain limit directly toward the cusp.

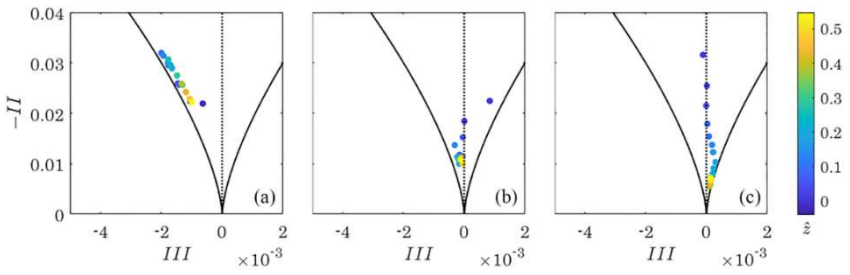

Figure 4. AIMs of Run 1 at Section 4 ($x/L_s = 0$): (a) $y/B_s = 0$, (b) 0.5, and (c) 1.00.

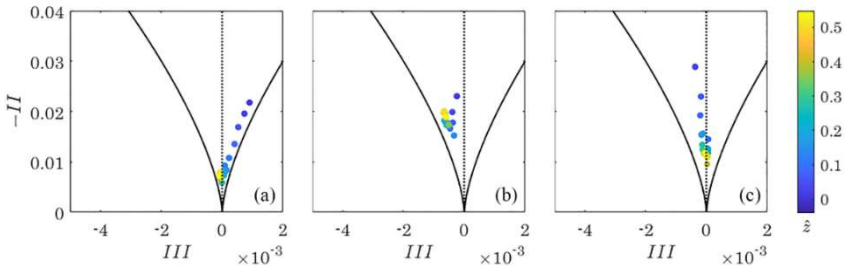

Figure 5. AIMs of Run 1 at Section 5 ($x/L_s = 1$): (a) $y/B_s = 0$, (b) 0.5, and (c) 1.00.

To investigate the effects of bed roughness, we show the AIMs for Run 3 at Sections 3, 4, and 5 in Figures 6, 7, and 8, respectively. The AIMs of Run 2, characterized by an intermediate bed roughness, are not reported here for brevity.

By analyzing Figures 6 to 8, it is evident that a higher roughness induces changes in the AIMs at each investigated Section. Looking at Figure 6a, upstream of and at the left side of the cylinder, moving from the crest level upwards, the data starting from the plane-strain limit tends to reach the 3D isotropy, and successively (from $z/h \sim 0.3$) the pancake-shaped turbulence. At the same time, Figure 6b shows that downstream of and at the left side of the cylinder data moves from the cigar-like turbulence to 3D isotropy, and successively toward the 2D turbulence (as the previous case, from $z/h \sim 0.3$), in which the stress ellipsoid tends to assume the shape of an elliptical disk. Thus, the higher roughness causes significant effects on the turbulence anisotropy at the flume centerline with respect to Run 1. The vertical distance equal to $z/h \sim 0.3$ appears like a cut-off point where the evolution of the turbulence anisotropy changes its behavior drastically.

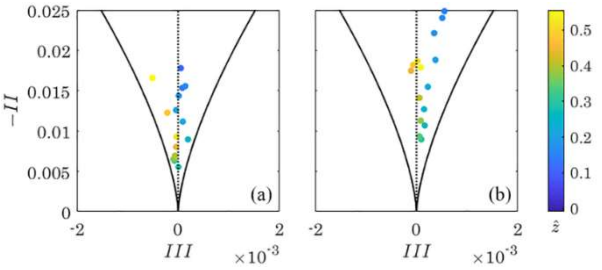

Figure 6. AIMs of Run 3 at Section 3 ($y/B_s = 0.33$): (a) $x/L_s = 0$, and (b) 1.00.

The effects of bed roughness are also noticeable looking at Figures 7 and 8. Specifically, at $x/L_s = 0$ and $y/B_s = 0$ (Fig. 7a), near the bed, turbulence is cigar-shaped. As the vertical distance from the bed increases, at first, it tends to be pancake-shaped and, subsequently, to the 3D isotropy. Finally, from $z/h \sim 0.3$ it seems to return back to the pancake-shaped state. In the meantime, at $x/L_s = 1$ and $y/B_s = 0$ (Fig. 8a), turbulence is initially cigar-shaped as in Run 1, but, starting again from $z/h \sim 0.3$, it tends to the 2D state (data moves along the plane-strain limit). Immediately upstream of the cylinder ($x/L_s = 0$, $y/B_s = 0.5$), Figure 7b shows a similar behavior to that of Figure 7a, with the following sequence in turbulence evolution starting from the bed: cigar shape, pancake shape, tendency to the 3D isotropy and, again from $z/h \sim 0.3$, pancake shape. The same occurs at the same spanwise distance, but downstream of the cylinder (Fig. 8b). However, in this case, after having shown a tendency to reach the cusp of the triangle, turbulence returns back to the initial state, which is the cigar-shaped turbulence. As regards the coordinates $x/L_s = 0$ and $y/B_s = 1$ (Fig. 7c) and $x/L_s = 1$ and $y/B_s = 1$ (Fig. 8c), data behaves in the same way as those with the lower bed roughness. This means that, in this area, turbulence anisotropy is governed by vegetation and the bed roughness has a limited effect on it.

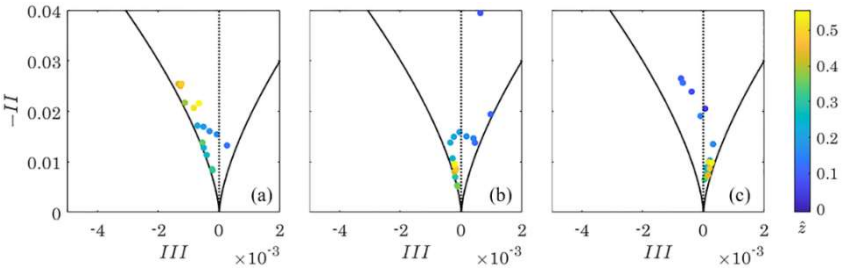

Figure 7. AIMs of Run 3 at Section 4 ($x/L_s = 0$): (a) $y/B_s = 0$, (b) 0.5, and (c) 1.00.

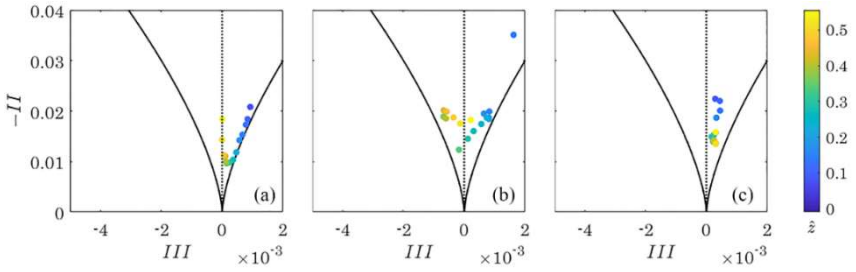

Figure 8. AIMs of Run 3 at Section 5 ($x/L_s = 1$): (a) $y/B_s = 0$, (b) 0.5, and (c) 1.00.

3.2 *Anisotropic invariant function*

To provide an insight on the turbulence anisotropy from the two-component limit to the isotropic one, Choi & Lumley (2001) defined the so-called anisotropic invariant function, F:

$$F = 1 + 9II + 27III \tag{4}$$

If anisotropy prevails, $F = 0$, whereas it equals 1 for 3D isotropic turbulence.

The distributions of F of the investigated Sections 1, 3, 4 and 5 for Runs 1 and 3 are shown in Figures 9 and 10, respectively. The results of Run 2 are not shown here for brevity. It is possible to note that the F distribution is quite uniform in the streamwise direction for both Sections 1 and 3, which are shown in Figures 9a and 9b. Instead, along the spanwise direction, upstream and downstream of the vegetation stem (Figs. 9c and 9d), the anisotropic invariant function varies, indicating that it is influenced by the position with respect to the cylinder. For all the Sections, it is evident that F gradually increases moving from the bed surface (where anisotropy prevails) toward the free surface (where turbulence tends to reach the 3D isotropic state). Thus, we can confirm that the bed roughness influence on turbulence anisotropy vanishes toward the free surface. However, looking at Figure 10 it is possible to deduce that a higher anisotropy degree characterizes the vertical distributions. Indeed, the variation of F along the streamwise direction is less uniform in the case of the higher bed roughness (Figs. 10a and 10b), and the same occurs also in the spanwise directions, as shown in Figures 10c and 10d.

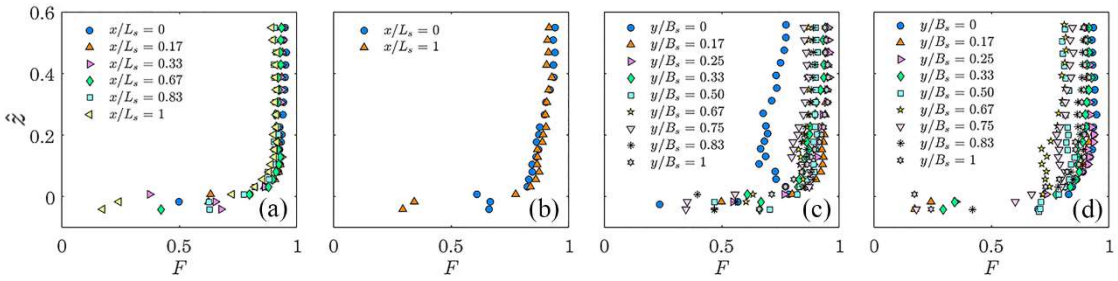

Figure 9. Vertical distributions of the anisotropic invariant function of Run 1 at: (a) Section 1 ($y/B_s = 0.17$): (b) Section 3 ($y/B_s = 0.33$), (c) Section 4 ($x/L_s = 0$), and (d) Section 5 ($x/L_s = 1$).

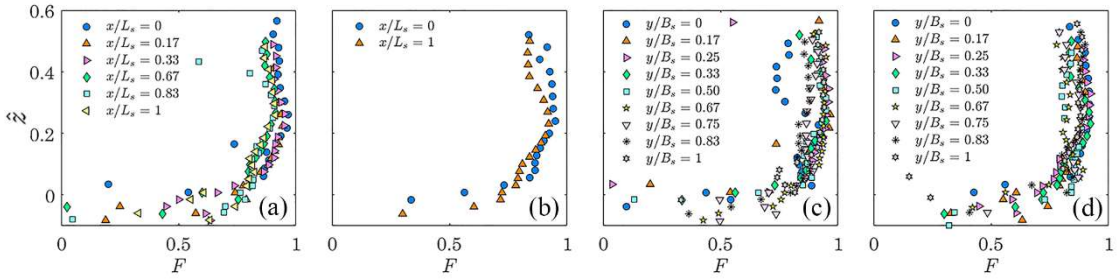

Figure 10. Vertical distributions of the anisotropic invariant function of Run 3 at: (a) Section 1 ($y/B_s = 0.17$): (b) Section 3 ($y/B_s = 0.33$), (c) Section 4 ($x/L_s = 0$), and (d) Section 5 ($x/L_s = 1$).

4 CONCLUSIONS

The turbulence anisotropy of flows through random and emergent rigid vegetation on three different rough beds, using the anisotropy invariant maps (AIMs) and the anisotropic invariant function, was investigated in this study. The principal findings can be summarized as follows.

1. The random arrangement of vegetation controls the evolution of the turbulence anisotropy near the bed, where the effect of bed roughness should be predominant. This is in contrast with the findings obtained in the same hydraulic conditions, but with vegetation having an aligned pattern.
2. By increasing the bed roughness, its effect on the turbulence anisotropy are visible in specific areas around the vegetation stem. Furthermore, the vertical distance equal to $z/h \sim 0.3$ appears like a cut-off point where the evolution of the turbulence anisotropy changes its behavior drastically. This is probably due to the combined effect of both bed roughness and vegetation.
3. Anisotropy prevails near the bed and it vanishes toward the free surface, where turbulence tends to reach the 3D isotropic state.
4. A higher bed roughness causes an irregular trend in the vertical distribution of the anisotropic invariant function in both the streamwise and spanwise directions.

The results obtained in this study could be useful for the calibration of numerical models based on the assumption of isotropic turbulence in the presence of random distributed vegetation within a river. This is an important aspect that cannot be neglected, since it may exert a strong impact on other phenomena, like the sediment transport processes in vegetated flows.

5 REFERENCES

Barman, J. & Kumar, B. 2022. Turbulence in a compound channel with the combination of submerged and emergent vegetation. *Physics of Fluids* 34(4):045114.

Caroppi, G., Gualtieri, P., Fontana, N. & Giugni, M. 2018. Vegetated channel flows: Turbulence anisotropy at flow–rigid canopy interface. *Geosciences* 8(7):259.

Choi, K.S. & Lumley, J.L. 2001. The return to isotropy of homogeneous turbulence. *Journal of Fluid Mechanics* 436:59-84.

Coscarella, F., Penna, N., Ferrante, A. P., Gualtieri, P. & Gaudio, R. 2021. Turbulent flow through random vegetation on a rough bed. *Water* 13(18):2564.

Dey, S. & Das, R. (2012). Gravel-bed hydrodynamics: Double-averaging approach. *Journal of Hydraulic Engineering* 138(8):707-725.

Dey, S., Paul, P., Ali, S. Z. & Padhi, E. 2020. Reynolds stress anisotropy in flow over two-dimensional rigid dunes. *Proceedings of the Royal Society A* 476(2242):20200638.

Emory, M. & Iaccarino, G. 2014. Visualizing turbulence anisotropy in the spatial domain with componentality contours. *Center for Turbulence Research: Annual Research Briefs* 123-138.

Goring, D.G. & Nikora, V.I. 2002. Despiking acoustic Doppler velocimeter data. *Journal of Hydraulic Engineering* 128(1):117-126.

Julien, P.Y. 2010. *Erosion and sedimentation*. Cambridge university Press: Cambridge, UK.

Lumley, J.L. & Newman, G.R. 1977. The return to isotropy of homogeneous turbulence. *Journal of Fluid Mechanics* 82(1):161-178.

Nepf, H.M. 2012. Flow and transport in regions with aquatic vegetation. *Annual Review of Fluid Mechanics* 44:123-142.

Penna, N., Coscarella, F., D'Ippolito, A. & Gaudio, R. 2020. Anisotropy in the free stream region of turbulent flows through emergent rigid vegetation on rough beds. *Water* 12(9):2464.

Penna, N., Coscarella, F., D'Ippolito, A. & Gaudio, R. 2022. Effects of fluvial instability on the bed morphology in vegetated channels. *Environmental Fluid Mechanics* 1-26.

Pope, S.B. 2000. *Turbulent Flows*. Cambridge University Press: Cambridge, UK.

Sarkar, S., Ali, S.Z. & Dey, S. 2019. Turbulence in Wall-Wake Flow Downstream of an Isolated Dunal Bedform. *Water* 11(10):1975.

Strom, K.B. & Papanicolaou, A.N. (2007). ADV measurements around a cluster microform in a shallow mountain stream. *Journal of Hydraulic Engineering* 133(12):1379-1389.